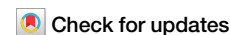


<https://doi.org/10.1038/s41524-025-01625-2>

Crystal-like thermal transport in amorphous carbon



Jaeyun Moon & Zhiting Tian

Thermal transport in amorphous carbon has attracted immense attention due to its extreme thermal properties: It has been reported to have among the highest thermal conductivity for bulk amorphous solids up to $\sim 37 \text{ W m}^{-1} \text{ K}^{-1}$, comparable to crystalline sapphire ($\alpha\text{-Al}_2\text{O}_3$). However, mechanism behind the high thermal conductivity remains elusive due to many variables at play. In this work, we perform large-scale ($\sim 10^5$ atoms) molecular dynamics simulations utilizing a machine learning potential based on neural networks with first-principles accuracy. Through spectral decomposition of thermal conductivity which enables a quantum correction to classical heat capacity, we find that propagating vibrational excitations govern thermal transport in amorphous carbon ($\sim 100\%$ of thermal conductivity) in sharp contrast to the convention that diffusive vibrational excitations dominate thermal transport in amorphous solids. This remarkable behavior resembles thermal transport in simple crystals. Our work, therefore, provides a perspective that deepens our understanding of intermediate thermal transport mechanisms between the two ends of spectrum of solids: crystalline and amorphous solids.

Vibrational properties of amorphous solids are of fundamental interest due to their anomalies compared to those of crystalline solids, including a Boson peak in the vibrational density of states^{1,2} and an excess heat capacity at cryogenic temperatures³. Combined with small average mean free paths on the order of interatomic distances⁴, these anomalies suggest different characteristics of vibrational heat carriers from those of phonons in simple crystals. Prior seminal works have proposed to categorize these heat carriers in amorphous solids as propagating, diffusive, and localized vibrations depending on their transport mechanisms^{5–7}. Propagating vibrational excitations are similar to phonons in that they have large mean free paths, thus transporting heat efficiently. However, due to disorder in amorphous solids, these propagating excitations exhibit vastly complex scattering mechanisms compared to phonon-phonon scattering in simple dielectric crystals including Akhiezer damping, thermally activated relaxation, Rayleigh scattering, and elastic heterogeneity scattering^{8–11}. Diffusive vibrations have ill-defined mean free paths below \sim interatomic distances and transport heat in a random walk manner. Localized vibrations are spatially localized and are often considered to contribute negligibly to thermal transport. These categorizations have been used to understand various thermal properties in numerous amorphous solids microscopically^{12–19}. Consensus is that diffusive vibrations govern thermal transport in most amorphous solids due to large degrees of disorder hindering propagation of vibrations, leading to low thermal conductivity in dielectric amorphous solids ($\lesssim 1 \text{ W m}^{-1} \text{ K}^{-1}$).

Recently, amorphous carbon has drawn immense attention due to its remarkable mechanical and thermal properties^{20–25}: Amorphous carbon

with similar density to crystalline diamond (3.5 g cm^{-3} at 300 K) can achieve larger Young's modulus and hardness than those of crystalline diamond²⁵ and it has among the highest thermal conductivity reported for pure bulk amorphous solids up to $\sim 37 \text{ W m}^{-1} \text{ K}^{-1}$ at 300 K, comparable to that of many crystalline solids such as sapphire^{22,26}. Numerous experimental^{22,27–29} and computational works^{30–33} have been conducted to elucidate the nature of atomic vibrations in amorphous carbon and to explore extreme thermal properties achievable in amorphous solids. Yet accurate understanding of thermal transport in amorphous carbon is still missing, as described below.

Prior measurements have shown that thermal conductivity has a strong positive correlation with mass density and sp^3 content, demonstrating that local atomic environment could be an important factor in thermal transport in amorphous carbon^{22,27–29}. However, thermal conductivity measurements of amorphous carbon vary significantly in literature (from ~ 1 to $\sim 37 \text{ W m}^{-1} \text{ K}^{-1}$) depending on many variables such as synthesis techniques and conditions that lead to different densities, sample qualities, and possible crystallinities. Accurate and systematic atomic simulation studies are, thus, necessary to microscopically understand the thermal transport mechanisms in amorphous carbon, and these will, in larger effect, play an essential role in understanding extreme thermal properties of amorphous solids.

Recent molecular dynamics simulations on amorphous carbon support the local structure (density and sp^3 content)-property (thermal conductivity) relationship^{30–33}. By categorizing vibrations into propagating and diffusive modes, these simulation works have further reported that diffusive vibrations play a substantial role in thermal conduction in amorphous

carbon (up to 70 % of thermal conductivity) at 300 K, a similar behavior observed in most other amorphous solids^{17,34,35}. However, these simulations report: 1. unphysically large vibrational density of states at high frequencies above ~70 THz similar to hydrogen vibrational frequencies using simple empirical potentials³⁰, 2. small simulation cells, comprised of hundreds to thousands of atoms, not able to adequately include low frequency vibrations^{30,31,33}, 3. classical thermal conductivity values at room temperatures where phonon occupation is inaccurately described below Debye temperatures (~2300 K for amorphous carbon)^{31,32}.

In this work, we perform molecular dynamics simulations of amorphous carbon using a machine learning potential based on neural networks. Large structures made of 110,592 atoms with varying densities from 3.0 to 3.8 g cm⁻³ are considered. With homogeneous non-equilibrium molecular dynamics descriptions of thermal conductivity based on a linear response theory, we decompose thermal conductivity into spectral contributions, enabling a quantum correction to the phonon occupation and heat capacity. The combination of machine learning potential with first principles accuracies, large structures, and quantum correction to heat capacity mitigates prior limitations mentioned before. By comparing with three widely used physical models and directly analyzing dispersions, we show that remarkably, propagating excitations govern thermal transport in amorphous carbon at room temperature (~100 % of thermal conductivity) similar to simple crystals. Our results demonstrate that a large presence of propagating excitations is crucial to achieve high thermal conductivity in amorphous solids and further provide a key insight into intermediate thermal transport mechanisms between crystalline and amorphous solids.

Results

Amorphous carbon structures

Representative amorphous solid structures at 3.0, 3.3, and 3.5 g cm⁻³ are shown in Fig. 1A. Molecular dynamics simulation details are discussed in Methods. Number of atoms having four nearest neighbors (*sp*³-bonded) increases with density. A negligible number of atoms had two or five neighbors. Cutoff distance of 1.85 Å was used to determine atomic coordination numbers^{36,37}. A large, spatially homogenous increase in the number of *sp*³-bonded atoms with increase in density is clearly visible. All *sp*³-bonded

atoms were subsequently identified for all structures and their density dependent population is plotted against prior experimental^{29,38–40} and computational works^{36,41} in Fig. 1B. While all data depict monotonic increase in *sp*³ population with density, some empirical potentials such as Tersoff³⁶ and Brenner⁴¹ underpredict the *sp*³ population by more than a half compared to experimental values. Structures based on machine-learning potentials such as Gaussian approximation potential (GAP)³⁶ and neuro-evolution potential (NEP) used here, appear to have more consistent *sp*³ population predictions against experiments and density functional theory (DFT) calculations. Resulting pair distribution function, $g(r) = \frac{1}{4\pi N r^2} \sum_{i,j} \langle \delta(r - |\mathbf{r}_i - \mathbf{r}_j|) \rangle$, is demonstrated for our 3.5 g cm⁻³ structure along with a prior DFT structure³⁶ at the same density in Fig. 1C. Here, N is the number of atoms, i is the number density, \mathbf{r}_i is the atomic position of the i th atom, and the angled brackets denotes an ensemble average. As expected for an amorphous solid, broad peaks and valleys are observed. Consistent pair distribution functions are demonstrated between the two curves.

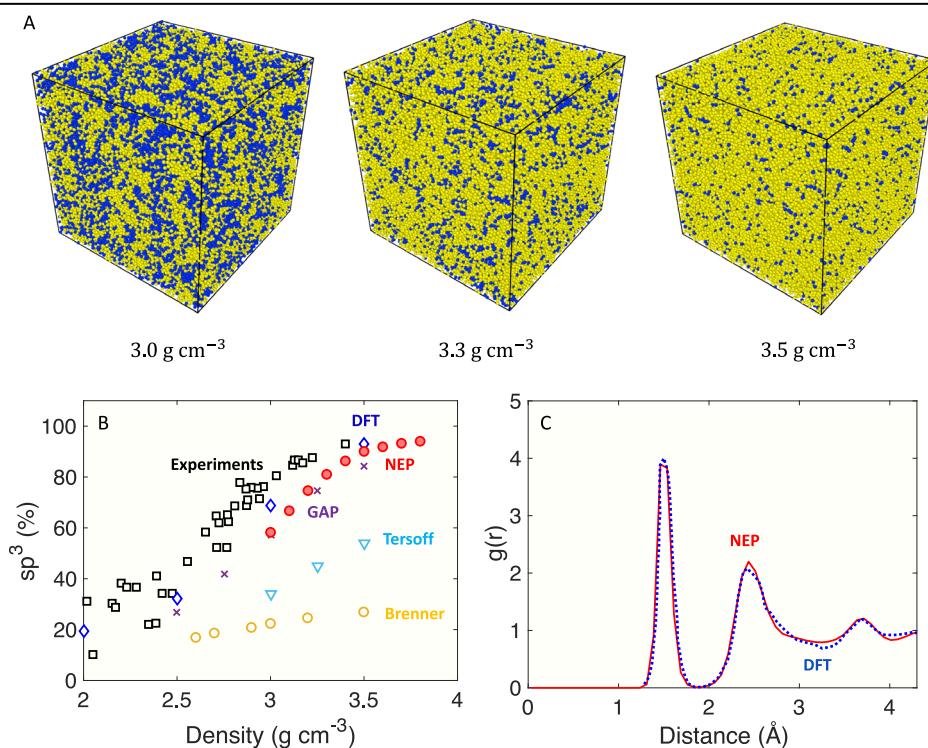
Vibrations in amorphous carbon

Using these structures, we next examine their vibrational densities of states (DOS) using spectral velocity autocorrelations (see Fig. 2)^{42–44}. Due to a large sample quantity typically required for density of states measurements, experimental measurement comparison is absent here. With increase in density, we observe a flatter DOS at low frequencies below 10 THz, which signifies higher Debye sound velocities (v_D) as DOS scales as v_D^{-3} . By fitting the Debye model of vibrational density of states below 5 THz, we obtain 12.97, 14.60, and 15.21 km s⁻¹ for the 3.0, 3.3, and 3.5 g cm⁻³ structures, respectively. Vibrational densities of states using the NEP potential appear to be more consistent with prior DFT calculations³⁷ while the DOS using a Tersoff potential³⁰ predicts a significant number of vibrations with frequencies higher than 50 THz. With the NEP potential, we then have structural and vibrational properties with first-principles accuracies for our large amorphous carbon structures.

Thermal conductivity and transport mechanisms

Thermal conductivity values for all the structures were then determined by homogeneous non-equilibrium molecular dynamics (HNEMD)^{45,46} (See

Fig. 1 | Structural properties of tetrahedral amorphous carbon. **A** Local atomic environment of tetrahedral amorphous carbon at different mass densities. Yellow and blue atoms denote atoms with *sp*³ and *sp*² hybridizations, respectively. At 3.0, 3.3, and 3.5 g cm⁻³, 58.3, 81.0, and 90.1 % of atoms are *sp*³-bonded, respectively. **B** Density dependent *sp*³ distributions of our NEP systems compared against previously reported values for various amorphous carbon systems from atomic simulations^{36,41} and experiments^{25,38–40}. **C** Pair distribution function of our system with 3.5 g cm⁻³ using the NEP potential (red curve) vs. prior literature using DFT³⁶ (blue curve).



“Methods”). Similar to the Green-Kubo (GK) formalism⁴⁷ in equilibrium molecular dynamics (EMD), the HNEMD method is based on a linear response theory. In HNEMD, independent phonon calculations are not required to obtain spectral thermal conductivity unlike other molecular dynamics based methodologies such as Green-Kubo modal analysis (GKMA)¹² and normal mode decomposition (NMD)⁴⁸ which limit the number of atoms due to large computational costs of constructing and diagonalizing dynamical matrices.

Classical and quantum corrected thermal conductivity of all systems studied here were plotted against experimental measurements and Green-Kubo thermal conductivity independently calculated here as shown in Fig. 3. Green-Kubo thermal conductivities were obtained by $k = \frac{1}{3k_BVT} \int_0^\infty dt \langle J(t) \cdot J(0) \rangle$ where $J(t)$ is the heat current. Classical thermal conductivity from HNEMD and GK thermal conductivity are within the error bars of each other.

There have been large variations in the measured thermal conductivities for amorphous carbon depending on the synthesis techniques, thickness, and sample quality. We observe that quantum corrected thermal conductivity for the amorphous carbon structures discussed here is on the same order of magnitude as some available measurements at 300 K^{27,28,49}. However, it is worth noting that these thermal conductivity values are smaller than the highest reported thermal conductivity value for amorphous carbon at $\sim 37 \text{ W m}^{-1} \text{ K}^{-1}$ ^{22,29}. Perhaps, the experimental samples could be nanocrystalline with apparent “amorphous” diffraction patterns as discussed in ref. 50, and the discrepancy merits further studies into this matter.

To see the effect of the quantum correction to the heat capacity on the total thermal conductivity in amorphous carbon, spectral thermal conductivity and thermal conductivity accumulation functions of 3.0, 3.3, and 3.5 g cm^{-3} structures at 300 K are shown in Fig. 3B and C, respectively. It appears that the effect of quantum correction to the specific heat on thermal conductivity becomes prominent above $\sim 7 \text{ THz}$. This is expected as $k_B T \sim 25 \text{ meV}$ or 6 THz at room temperature. At 300 K, the quantum correction to the heat capacity reduces the classical thermal conductivities by as much as 30 to 40 %, demonstrating the importance of considering quantum effects in these materials. Further, it is interesting to note that density affects spectral thermal conductivity of amorphous carbon drastically below $\sim 10 \text{ THz}$ while there is little to no effect above 10 THz . Our temperature-dependent thermal conductivity studies discussed in Supplementary Information further suggest that these low-frequency vibrations have temperature-dependent scattering rates. Therefore, our work reveals that density-dependent thermal conductivity in amorphous carbon widely observed in literature at room temperature is likely due to changes in transport properties of these temperature-sensitive low-frequency vibrations.

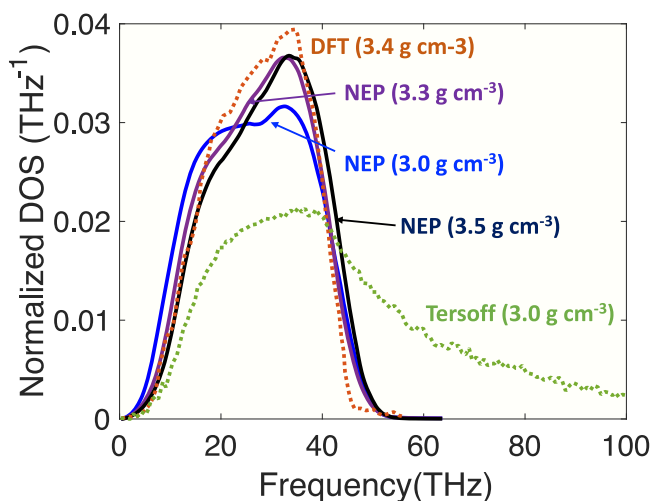
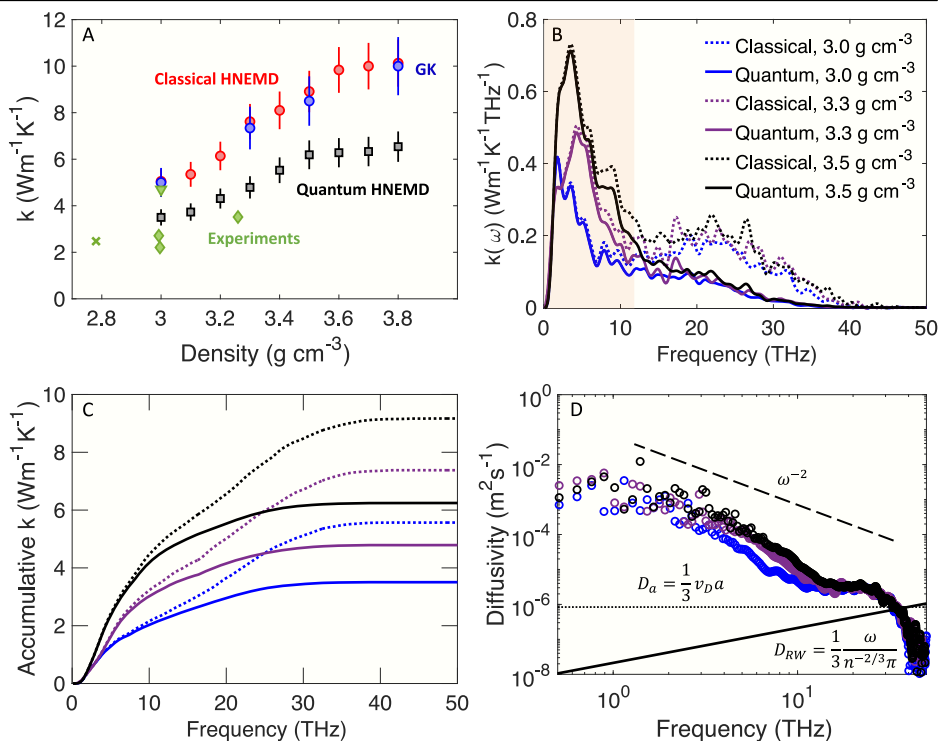


Fig. 2 | Vibrational densities of states (DOS) of various amorphous carbon systems. DOS for the 3.0, 3.3, and 3.5 g cm^{-3} structures studied here are shown as solid blue, purple, and black curves, respectively. DFT calculations (3.4 g cm^{-3}) are shown as a brown dotted curve, and DOS using Tersoff potential (3.0 g cm^{-3}) is depicted as a green dotted curve.

Discussion

We next examine spectral thermal diffusivity values for the 3.0, 3.3, and 3.5 g cm^{-3} structures at 300 K obtained by $D(\omega) = \frac{k(\omega)}{C(\omega)DOS(\omega)}$ as plotted in Fig. 3D along with some widely used diffusivity models for amorphous materials. Due to lack of clear consensus on the definition of propagating vs.

Fig. 3 | Thermal transport properties of amorphous carbon. **A** Density dependent classical (red solid circles) and quantum mechanical (black solid squares) thermal conductivity at 300 K compared against thermal conductivity values using Green-Kubo formalism (blue solid circles) and available measurements (green symbols). Sample synthesis techniques and thickness are: cross (filtered arc, 47 nm)²⁸, diamond (filtered cathodic vacuum arc, 18.5–100 nm)²⁷, and inverse triangle (filtered cathodic vacuum arc, 20–100 nm)⁴⁹. **B** Classical (solid curves) and quantum mechanical (dotted curves) spectral thermal conductivity. Shaded orange region highlights large density dependence in spectral thermal conductivity. **C** Thermal conductivity accumulation function of 3.0, 3.3, and 3.5 g cm^{-3} structures at 300 K. Thermal conductivity saturates above $\sim 30 \text{ THz}$. **D** Spectral diffusivity of 3.0, 3.3, and 3.5 g cm^{-3} structures at 300 K. Color schemes in (C) and (D) are the same as (B). Dashed line representing the inverse quadratic power law is a guide to the eye. Dotted line represents diffusivity D_a when the mean free path is interatomic distance. Solid black line depicts a diffusivity based on a random-walk theory D_{RW} .



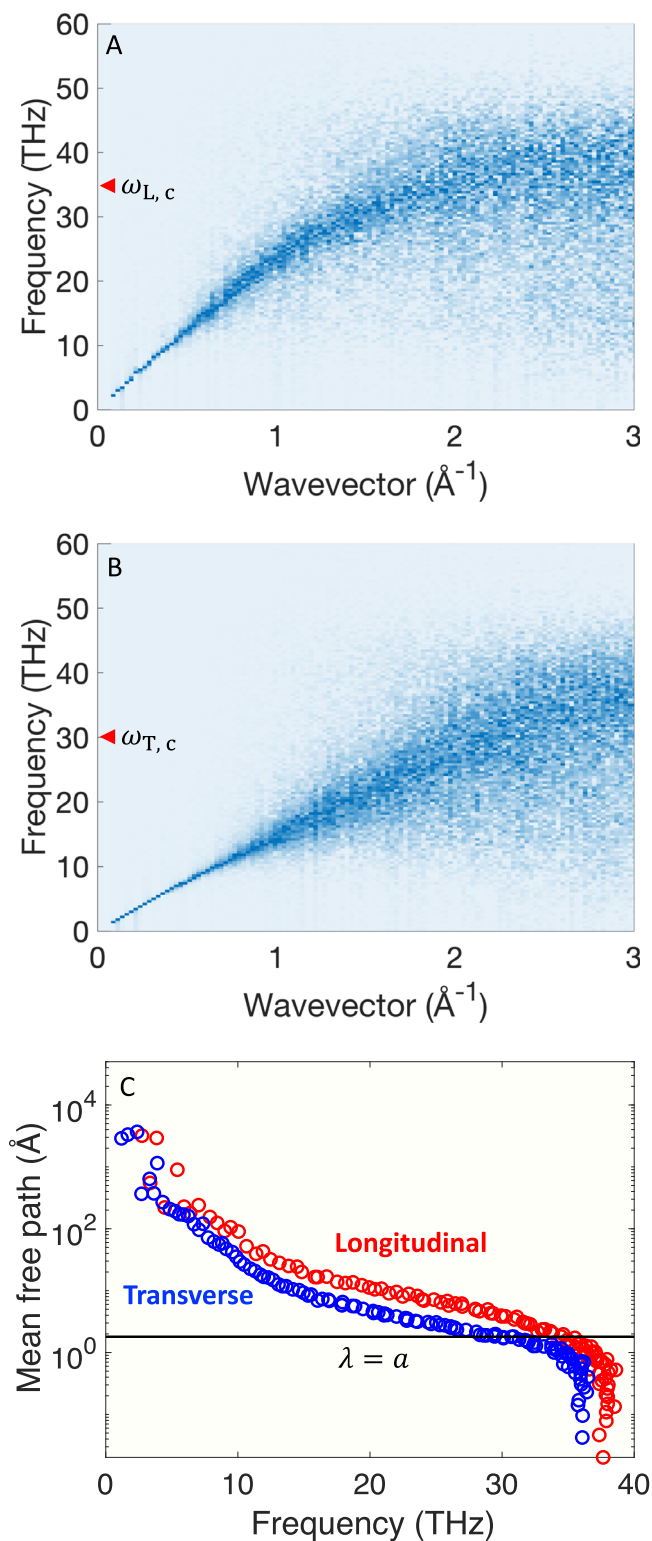


Fig. 4 | Vibrational dispersion and mean free paths for the 3.5 g cm⁻³ structure. Wavevector and frequency resolved (A) longitudinal and (B) transverse velocity current correlations. Estimated crossover frequencies from propagating to diffusive vibrations are noted as $\omega_{L,c}$ and $\omega_{T,c}$ for longitudinal and transverse directions, respectively. C Extracted mean free paths (λ) for both longitudinal (red circles) and transverse (blue circles) excitations. Horizontal black line is a guide to eye representing λ approaching interatomic distance (a) of amorphous carbon.

diffusive vibrations, there currently exist a few different proposed methods to distinguish these two behaviors. Some methods require solving the dynamical matrices and subsequently examine normal mode shapes or properties (e.g., eigenvector periodicity⁵¹), and the other methods rely on physical models that describe propagating and diffusive vibrations. The first route is not computationally feasible here. Our systems ($\sim 10^5$ atoms) are more than an order of magnitude larger than typical numbers of atoms used for dynamical matrix calculations using simple empirical potentials in literature (10^3 – 10^4 atoms)^{15,16,31}. Therefore, we first resort to physical models describing propagating and diffusive vibrations.

The first model relies on how propagating wave lifetimes depend on frequency. At THz frequencies, lifetimes of propagating vibrations typically follow ω^{-2} , whereas at lower frequencies, the power law follows more complex frequency dependencies including Rayleigh scattering ($\sim \omega^{-4}$)^{52–56}. Prior works determined the frequency at which ω^{-2} dependence in lifetimes and diffusivity disappears as the transition frequency from propagating to diffusive vibrations in amorphous solids including amorphous carbon^{15,30,35}. Using this criterion, we find that the transition frequency can be approximated to be around ~ 32 THz for these amorphous carbon structures (See Fig. S1 for more details in Supplementary Information).

The second physical model considers the lowest diffusivity (D_a) possible by a propagating wave where group velocity is sound velocity (here, we use the Debye velocity of ~ 14 km s⁻¹ as an average value) and mean free path is the interatomic distance, a . The third model considered here considers maximum diffusivity for diffusive vibrations and is derived from a random walk theory⁵⁷ that has a linear dependence on frequency as $D_{RW} = \frac{1}{3} \frac{v}{n} \omega$ where n is the number density. If physically realistic, these two independent models should ideally merge at a certain frequency for amorphous carbon. These two criteria have been previously used in amorphous solids but also in complex crystals to determine propagating vs. diffusive normal modes that resulted in consistent thermal conductivity with experiments^{16,55,58,59}. Applying these two physical models leads to nearly identical crossover frequencies at ~ 35 THz in amorphous carbon as shown in Fig. 3D.

Three physical models considered here consistently lead to remarkably high crossover frequencies of ~ 30 – 35 THz. For these propagating vibrational excitations then, crisp dispersions with well-defined frequencies, group velocities, and mean free paths should be observed^{1,53,60–62}. Representative longitudinal and transverse dispersions for the 3.5 g cm⁻³ amorphous carbon structure are shown in Fig. 4A and B (see “Methods” for calculation details). At first glance, clear dispersions are demonstrated up to ~ 30 THz and ~ 20 THz for longitudinal and transverse excitations, respectively. By carefully fitting the single damped harmonic oscillator model at each wavevector shown in Fig. S2 in the Supplementary Information, we report mean free paths of longitudinal and transverse excitations in Fig. 4C. We find that propagating to diffusive crossover frequencies for longitudinal and transverse excitations are in a similar range as the other physical models at ~ 30 and 35 THz, respectively. Further, the mean free paths vary by nearly four orders of magnitude from ~ 1 THz to the crossover frequencies, similar to spectral thermal diffusivity calculated by HNEMD as shown in Fig. 3D.

All evidences based on the three physical models and dispersion analysis point to the conclusion that despite the disordered structures, propagating vibrations below 30–35 THz dictate thermal transport (~ 100 % of thermal conductivity) in amorphous carbon at 300 K as demonstrated in Fig. 3C where thermal conductivity accumulation saturates at ~ 30 THz. The fact that the propagating vibrations dominate heat conduction here surprisingly resembles thermal transport in simple dielectric crystals such as crystalline silicon despite different scattering mechanisms. For crystals with ultra-low thermal conductivity, inclusion of diffuson-like thermal transport is often necessary to interpret their overall thermal transport. Despite their strong temperature dependence, these crystals have been described as having glass-like thermal transport⁶³. Correspondingly, we characterize thermal transport in amorphous carbon as having crystal-like thermal transport.

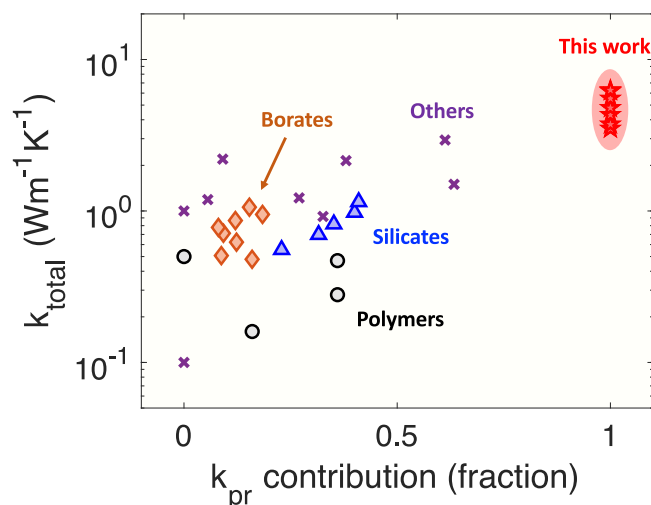


Fig. 5 | Survey of reported contributions to thermal conductivity at 300 K from propagating vibrational excitations in various amorphous solids. Amorphous polymers (black circles) shown are polyethylene^{67,68}, polystyrene⁶⁷, and polypropylene⁶⁷. Silicates (blue triangles) and borates (brown diamonds) include various alkali and alkaline earth metal modifier cations¹⁸. Denoted as others (purple crosses) include niobium pentoxide⁶⁹, silicon^{15,35}, calcium-silicate-hydrates³⁵, silicon nitride⁷⁰, hafnia⁷¹, silicon carbide⁷², silicon telluride¹⁹, lanthanum magnesium hexaaluminate⁷³, and silica⁷⁴.

Our results on amorphous carbon are demonstrated clearly in context of many other amorphous solids ranging from polymers to nitrides and oxides shown in Fig. 5. In many of those works presented, similar approaches to estimate propagating vs. diffusive vibrations as discussed here have been adopted. It is clear that most amorphous solids reported have a low thermal conductivity below $\sim 1 \text{ W m}^{-1} \text{ K}^{-1}$, and diffusive vibrations dictate the thermal transport. From the prior literature studies, there appear to be three systematically “forbidden” regions in the thermal conductivity space for amorphous solids: a void of amorphous materials with low thermal conductivities below $\sim 1 \text{ W m}^{-1} \text{ K}^{-1}$ with high contributions from propagating excitations, lack of high thermal conductivity amorphous solids above $\sim 1\text{--}2 \text{ W m}^{-1} \text{ K}^{-1}$ where diffusive vibrations dominate, and high thermal conductivity amorphous solids where propagating vibrations govern thermal transport. Through amorphous carbon, we show that the latter is now realizable despite amorphous structure hindering propagation of vibrations. One promising strategy to potentially achieve high thermal conductivity in non-metallic amorphous materials, therefore, lies in having large presence of propagating excitations and perhaps, further engineering their scattering mechanisms.

Using a machine learning potential based on neural networks for large-scale molecular dynamics simulations on amorphous carbon, we elucidate the microscopic mechanism behind its high thermal conductivity values, among the highest in amorphous solids. Through spectral decomposition of thermal conductivity, quantum correction to the heat capacity, and dispersion analysis, we demonstrate that propagating vibrational excitations, present up to 30–35 THz, dictate thermal transport in amorphous carbon at room temperature ($\sim 100\%$ of thermal conductivity), reminiscent of phonons in simple dielectric crystals. Via a survey of thermal transport literature on ~ 30 amorphous solids, we suggest that having a dominant presence of propagating excitations is key to achieving extreme thermal conductivities in amorphous solids.

Methods

Molecular dynamics simulations

Crystal diamond of 110,592 atoms at various densities from 3.0 to 3.8 g cm^{-3} were melted at 15,000 K for 30 ps, followed by quenching to an amorphous state at 1000 K at 100 K ps^{-1} in NVT ensemble (constant number of atoms,

volume, and temperature) using Graphics Processing Units Molecular Dynamics (GPUMD)⁶⁴. Resulting structures were then annealed for 1 ns at 1000 K and were subsequently cooled to 300 K at 100 K ps^{-1} in NVT. Using these seed structures, molecular dynamics outputs were recorded for 2 ns after initial equilibration of 1 ns at desired temperatures under NVT. Our large structures result in more statistics of propagating vibrational excitations compared to prior molecular dynamics simulations with thousands of atoms^{30,31}. A timestep of 1 fs was used. Three runs with different initial velocities were carried out for better statistics for thermal and vibrational property calculations. Neuro-evolution potential (NEP), a neural network based machine-learning potential, was utilized to describe interatomic interactions with first-principles accuracies^{64,65}. The NEP potential used here was previously trained from 4080 carbon structures including bulk crystalline, liquid, and amorphous structures as well as amorphous surfaces and isolated dimer structures⁶⁴. The testing data set had 450 carbon structures. Root mean square errors in energy and forces between NEP predictions and target values were comparable to results using other types of machine learning potential for the carbon structures such as Gaussian Approximation Potential (GAP) and Recursive Embedded-atom Neural Network (REANN).

Thermal conductivity calculations

In HNEMD, one applies an external driving force perturbation and examines the materials response (heat current) to it as

$$\mathbf{F}_i^{\text{ext}} = \mathbf{F}_e \cdot \mathbf{W}_i \quad (1)$$

where \mathbf{F}_e is the driving force parameter with the dimension of inverse length, $\mathbf{W}_i = \sum_{j \neq i} \frac{\partial U_j}{\partial \mathbf{r}_{ij}} \otimes \mathbf{r}_{ij}$ is the 3 by 3 virial tensor of an atom, \otimes represents a tensor product, and U_j is the atomic potential energy. A small value of \mathbf{F}_e at $2 \times 10^{-4} \text{ \AA}^{-1}$ was used to ensure the system is in the linear response regime.

Instantaneous heat current is related to the virial tensor by

$$\mathbf{J}(t) = \sum_i \mathbf{W}_i \cdot \mathbf{v}_i \quad (2)$$

Ensemble average of the heat current is then directly related to the driving force parameter and thermal conductivity by

$$\langle J^\alpha \rangle = TV \sum_\beta k^{\alpha\beta} F_e^\beta \quad (3)$$

where α and β represent Cartesian directions, T is temperature, and V is system volume. Thermal conductivity can therefore be determined from Eqs. (1) to (3). For isotropic systems like amorphous carbon, isotropic thermal conductivity is expected. Therefore, we generally refer to thermal conductivity as k . We can further decompose thermal conductivity into spectral contributions through virial-velocity function $Q(t) = \sum_i \langle \mathbf{W}_i(0) \cdot \mathbf{v}_i(t) \rangle$ as

$$k(\omega) = \frac{2}{VTF_e} \int_{-\infty}^{\infty} Q(t) e^{i\omega t} dt \quad (4)$$

Due to the classical nature of molecular dynamics simulations, atomic dynamics follows the Maxwell-Boltzmann distribution. With spectral thermal conductivity, one could, therefore, apply a spectral ‘quantum correction’ to the occupation number and heat capacity such that

$$k_Q(\omega) = k(\omega) \frac{x^2 e^x}{(e^x - 1)^2} \quad (5)$$

where $x = \frac{\hbar\omega}{k_B T}$, \hbar is the reduced Planck constant, and k_B is the Boltzmann constant⁶⁶. HNEMD and spectral decompositions of thermal conductivity have been utilized in various materials including graphene⁴⁶ and amorphous silicon⁶⁶.

Dispersion analysis

Longitudinal and transverse dispersions from wavevector and frequency resolved velocity current correlations for amorphous carbon were obtained by^{1,16,53,60}

$$C_{L,T}(q, \omega) = \frac{q^2}{2\pi\omega^2 N} \int dt \langle \mathbf{j}_{L,T}(q, t) \cdot \mathbf{j}_{L,T}(-q, 0) \rangle e^{i\omega t} \quad (6)$$

where subscripts, L , T , refer to longitudinal or transverse branches, q is the wavevector, ω is the radial frequency, and $\mathbf{j}_{L,T}(q, t)$ is given by

$$\mathbf{j}_L(q, t) = \sum_i^N (\mathbf{v}_i(t) \cdot \hat{\mathbf{q}}) \hat{\mathbf{q}} e^{i\mathbf{q} \cdot \mathbf{r}_i(t)} \quad (7)$$

$$\mathbf{j}_T(q, t) = \sum_i^N (\mathbf{v}_i(t) - (\mathbf{v}_i(t) \cdot \hat{\mathbf{q}}) \hat{\mathbf{q}}) e^{i\mathbf{q} \cdot \mathbf{r}_i(t)} \quad (8)$$

with $\mathbf{v}_i(t)$, $\mathbf{r}_i(t)$, and $\hat{\mathbf{q}}$ representing atomic velocities, positions, and unit wavevector, respectively.

Data availability

All data supporting the findings of this study are available within the article and its Supplementary Information. All other data are available from the corresponding author upon request.

Received: 9 January 2025; Accepted: 26 April 2025;

Published online: 17 May 2025

References

- Shintani, H. & Tanaka, H. Universal link between the boson peak and transverse phonons in glass. *Nat. Mater.* **7**, 870–877 (2008).
- Chumakov, A. et al. Role of disorder in the thermodynamics and atomic dynamics of glasses. *Phys. Rev. Lett.* **112**, 025502 (2014).
- Zeller, R. C. & Pohl, R. O. Thermal conductivity and specific heat of noncrystalline solids. *Phys. Rev. B* **4**, 2029 (1971).
- Kittel, C. Interpretation of the thermal conductivity of glasses. *Phys. Rev.* **75**, 972–974 (1949).
- Allen, P. B. & Feldman, J. L. Thermal conductivity of glasses: theory and application to amorphous Si. *Phys. Rev. Lett.* **62**, 645 (1989).
- Allen, P. B., Feldman, J. L., Fabian, J. & Wooten, F. Diffusons, locons and propagons: character of atomic vibrations in amorphous Si. *Philos. Mag. B* **79**, 1715–1731 (1999).
- Allen, P. B., Garber, W. & Angelani, L. Character of atomic vibrations in a Lennard-Jones glass (2003). ArXiv:cond-mat/0307435.
- Rayleigh, J. W. S. B. *The Theory of Sound* (Macmillan, 1896).
- Schirmacher, W., Ruocco, G. & Scopigno, T. Acoustic attenuation in glasses and its relation with the Boson peak. *Phys. Rev. Lett.* **98**, 025501 (2007).
- Nava, R., Vecchi, M. P., Romero, J. & Fernández, B. Akhiezer damping and the thermal conductivity of pure and impure dielectrics. *Phys. Rev. B* **14**, 800–807 (1976).
- Phillips, W. A. Tunneling states in amorphous solids. *J. Low. Temp. Phys.* **7**, 351–360 (1972).
- Lv, W. & Henry, A. Direct calculation of modal contributions to thermal conductivity via Green-Kubo modal analysis. *N. J. Phys.* **18**, 013028 (2016).
- Lv, W. & Henry, A. Examining the validity of the phonon gas model in amorphous materials. *Sci. Rep.* **6**, 37675 (2016).
- Lv, W. & Henry, A. Non-negligible contributions to thermal conductivity from localized modes in amorphous silicon dioxide. *Sci. Rep.* **6**, 35720 (2016).
- Larkin, J. M. & McGaughey, A. J. H. Thermal conductivity accumulation in amorphous silica and amorphous silicon. *Phys. Rev. B* **89**, 144303 (2014).
- Moon, J., Latour, B. & Minnich, A. J. Propagating elastic vibrations dominate thermal conduction in amorphous silicon. *Phys. Rev. B* **97**, 024201 (2018).
- DeAngelis, F. et al. Thermal transport in disordered materials. *Nanoscale Microscale Thermophys. Eng.* **23**, 81–116 (2018).
- Sørensen, S. S. et al. Heat conduction in oxide glasses: balancing diffusons and propagons by network rigidity. *Appl. Phys. Lett.* **117**, 031901 (2020).
- Aryana, K. et al. Tuning network topology and vibrational mode localization to achieve ultralow thermal conductivity in amorphous chalcogenides. *Nat. Commun.* **12**, 2817 (2021).
- Zeng, X. et al. Pressure effect on elastic constants and related properties of Ti3Al intermetallic compound: a first-principles study. *Materials* **11**, 2015 (2018).
- Lin, Y. et al. Amorphous diamond: a high-pressure superhard carbon allotrope. *Phys. Rev. Lett.* **107**, 175504 (2011).
- Shang, Y. et al. Enhancement of short/medium-range order and thermal conductivity in ultrahard sp³ amorphous carbon by C70 precursor. *Nat. Commun.* **14**, 7860 (2023).
- Zhang, S. et al. Discovery of carbon-based strongest and hardest amorphous material. *Natl. Sci. Rev.* **9**, nwab140 (2022).
- Zhang, S. et al. Narrow-gap, semiconducting, superhard amorphous carbon with high toughness, derived from C60 fullerene. *Cell Rep. Phys. Sci.* **2**, 100575 (2021).
- Shang, Y. et al. Ultrahard bulk amorphous carbon from collapsed fullerene. *Nature* **599**, 599–604 (2021).
- Cahill, D. G., Lee, S.-M. & Selinder, T. I. Thermal conductivity of {κ}-Al₂O₃ and {α}-Al₂O₃ wear-resistant coatings. *J. Appl. Phys.* **83**, 5783–5786 (1998).
- Shamsa, M. et al. Thermal conductivity of diamond-like carbon films. *Appl. Phys. Lett.* **89**, 161921 (2006).
- Bullen, A. J., O'Hara, K. E., Cahill, D. G., Monteiro, O. & von Keudell, A. Thermal conductivity of amorphous carbon thin films. *J. Appl. Phys.* **88**, 6317–6320 (2000).
- Shang, B., Guan, P. & Barrat, J.-L. Elastic avalanches reveal marginal behavior in amorphous solids. *Proc. Natl Acad. Sci.* **117**, 86–92 (2020).
- Lv, W. & Henry, A. Phonon transport in amorphous carbon using Green-Kubo modal analysis. *Appl. Phys. Lett.* **108**, 181905 (2016).
- Giri, A., Dionne, C. J. & Hopkins, P. E. Atomic coordination dictates vibrational characteristics and thermal conductivity in amorphous carbon. *npj Comput. Mater.* **8**, 1–7 (2022).
- Suarez-Martinez, I. & Marks, N. A. Effect of microstructure on the thermal conductivity of disordered carbon. *Appl. Phys. Lett.* **99**, 033101 (2011).
- Minamitani, E., Shiga, T., Kashiwagi, M. & Obayashi, I. Relationship between local coordinates and thermal conductivity in amorphous carbon. *J. Vac. Sci. Technol. A* **40**, 033408 (2022).
- Moon, J. & Minnich, A. J. Sub-amorphous thermal conductivity in amorphous heterogeneous nanocomposites. *RSC Adv.* **6**, 105154–105160 (2016).
- Zhou, Y., Morshedifard, A., Lee, J. & Abdolhosseini Qomi, M. J. The contribution of propagons and diffusons in heat transport through calcium-silicate-hydrates. *Appl. Phys. Lett.* **110**, 043104 (2017).
- Deringer, V. L. & Csányi, G. Machine learning based interatomic potential for amorphous carbon. *Phys. Rev. B* **95**, 094203 (2017).
- Sosso, G. C., Deringer, V. L., Elliott, S. R. & Csányi, G. Understanding the thermal properties of amorphous solids using machine-learning-based interatomic potentials. *Mol. Simul.* **44**, 866–880 (2018).
- Schwan, J. et al. Tetrahedral amorphous carbon films prepared by magnetron sputtering and DC ion plating. *J. Appl. Phys.* **79**, 1416–1422 (1996).
- Fallon, P. J. et al. Properties of filtered-ion-beam-deposited diamondlike carbon as a function of ion energy. *Phys. Rev. B* **48**, 4777–4782 (1993).

40. Ferrari, A. C. et al. Density, sp³ fraction, and cross-sectional structure of amorphous carbon films determined by X-ray reflectivity and electron energy-loss spectroscopy. *Phys. Rev. B* **62**, 11089–11103 (2000).
41. Pastewka, L., Pou, P., Pérez, R., Gumbsch, P. & Moseler, M. Describing bond-breaking processes by reactive potentials: Importance of an environment-dependent interaction range. *Phys. Rev. B* **78**, 161402 (2008).
42. Moon, J., Lindsay, L. & Egami, T. Atomic dynamics in fluids: normal mode analysis revisited. *Phys. Rev. E* **108**, 014601 (2023).
43. Grest, G. S., Nagel, S. R. & Rahman, A. Density of states and the velocity autocorrelation function derived from quench studies. *J. Chem. Phys.* **74**, 4 (1981).
44. Moon, J. *Heat Carriers in Liquids: An Introduction* (Springer, 2024).
45. Fan, Z., Dong, H., Harju, A. & Ala-Nissila, T. Homogeneous nonequilibrium molecular dynamics method for heat transport and spectral decomposition with many-body potentials. *Phys. Rev. B* **99**, 064308 (2019).
46. Gabourie, A. J., Fan, Z., Ala-Nissila, T. & Pop, E. Spectral decomposition of thermal conductivity: comparing velocity decomposition methods in homogeneous molecular dynamics simulations. *Phys. Rev. B* **103**, 205421 (2021).
47. Kubo, R. The fluctuation-dissipation theorem. *Rep. Prog. Phys.* **29**, 255 (1966).
48. McGaughey, A. J. & Larkin, J. M. Predicting phonon properties from equilibrium molecular dynamics simulations. *Ann. Rev. Heat. Transf.* **17**, 49–87 (2014).
49. Chen, G., Hui, P. & Xu, S. Thermal conduction in metalized tetrahedral amorphous carbon (ta-C) films on silicon. *Thin Solid Films* **366**, 95–99 (2000).
50. Treacy, M. M. J. & Borisenko, K. B. The local structure of amorphous silicon. *Science* **335**, 950–953 (2012).
51. Seyf, H. R. & Henry, A. A method for distinguishing between propagons, diffusions, and locons. *J. Appl. Phys.* **120**, 025101 (2016).
52. Fiorentino, A., Drigo, E., Baroni, S. & Pegolo, P. Unearthing the foundational role of anharmonicity in heat transport in glasses. *Phys. Rev. B* **109**, 224202 (2024).
53. Monaco, G. & Mossa, S. Anomalous properties of the acoustic excitations in glasses on the mesoscopic length scale. *Proc. Natl Acad. Sci.* **106**, 16907–16912 (2009).
54. Monaco, G. & Giordano, V. M. Breakdown of the Debye approximation for the acoustic modes with nanometric wavelengths in glasses. *Proc. Natl Acad. Sci. USA* **106**, 3659–3663 (2009).
55. Kim, T., Moon, J. & Minnich, A. J. Origin of micrometer-scale propagation lengths of heat-carrying acoustic excitations in amorphous silicon. *Phys. Rev. Mater.* **5**, 065602 (2021).
56. Ferrante, C. et al. Acoustic dynamics of network-forming glasses at mesoscopic wavelengths. *Nat. Commun.* **4**, 1793 (2013).
57. Agne, M. T., Hanus, R. & Snyder, G. J. Minimum thermal conductivity in the context of *diffuson*-mediated thermal transport. *Energy Environ. Sci.* **11**, 609–616 (2018).
58. Luo, Y., Yang, X., Feng, T., Wang, J. & Ruan, X. Vibrational hierarchy leads to dual-phonon transport in low thermal conductivity crystals. *Nat. Commun.* **11**, 2554 (2020).
59. Cai, Z., Lin, S., Ahmadian-Yazdi, M.-R. & Zhao, C. Diffuson-dominated and ultra defect-tolerant two-channel thermal transport in hybrid halide perovskites. *Adv. Funct. Mater.* **34**, 2307648 (2023).
60. Moon, J. et al. Thermal acoustic excitations with atomic-scale wavelengths in amorphous silicon. *Phys. Rev. Mater.* **3**, 065601 (2019).
61. Sette, F., Krisch, M. H., Masciovecchio, C., Ruocco, G. & Monaco, G. Dynamics of glasses and glass-forming liquids studied by inelastic X-ray scattering. *Science* **280**, 1550–1555 (1998).
62. Fiorentino, A., Pegolo, P. & Baroni, S. Hydrodynamic finite-size scaling of the thermal conductivity in glasses. *npj Comput. Mater.* **9**, 1–11 (2023).
63. Mukhopadhyay, S. et al. Two-channel model for ultralow thermal conductivity of crystalline Ti₃VSe₄. *Science* **360**, 1455–1458 (2018).
64. Fan, Z. et al. GPUMD: a package for constructing accurate machine-learned potentials and performing highly efficient atomistic simulations. *J. Chem. Phys.* **157**, 114801 (2022).
65. Fan, Z. et al. Neuroevolution machine learning potentials: combining high accuracy and low cost in atomistic simulations and application to heat transport. *Phys. Rev. B* **104**, 104309 (2021).
66. Wang, Y., Fan, Z., Qian, P., Caro, M. A. & Ala-Nissila, T. Quantum-corrected thickness-dependent thermal conductivity in amorphous silicon predicted by machine learning molecular dynamics simulations. *Phys. Rev. B* **107**, 054303 (2023).
67. Feng, T. et al. Size effects in the thermal conductivity of amorphous polymers. *Phys. Rev. Appl.* **14**, 044023 (2020).
68. Cai, Z., Lin, S. & Zhao, C. Anomalous diffusion and locon-dominated wigner multi-channel thermal transport in disordered and shear-aligned polymers. *Macromolecules* **57**, 6209–6220 (2024).
69. Cheng, Z. et al. Diffuson-driven ultralow thermal conductivity in amorphous Nb₂O₅ thin films. *Phys. Rev. Mater.* **3**, 025002 (2019).
70. Tambo, N. et al. Ultimate suppression of thermal transport in amorphous silicon nitride by phononic nanostructure. *Sci. Adv.* **6**, eabc0075 (2020).
71. Zhang, H., Wei, H. & Bao, H. Thermal transport mechanism of amorphous HfO₂: a molecular dynamics based study. *J. Therm. Sci.* **31**, 1052–1060 (2022).
72. Thakur, S. et al. Density and atomic coordination dictate vibrational characteristics and thermal conductivity of amorphous silicon carbide. *Phys. Rev. Mater.* **6**, 094601 (2022).
73. Huang, W., Che, J., Wang, X. & Peng, N. Thermal transport properties and lattice vibration modes in crystalline and amorphous LaMgAl₁₁O₁₉. *J. Alloy. Compd.* **955**, 170245 (2023).
74. Zhu, X. & Shao, C. Effect of anharmonicity on the thermal conductivity of amorphous silica. *Phys. Rev. B* **106**, 014305 (2022).

Acknowledgements

Z.T. acknowledges the support of the Department of the Navy, Office of Naval Research under ONR award number N00014-22-1-2357. We are grateful for discussions with Dr. Lucas Lindsay. This work used the Advanced Cyberinfrastructure Coordination Ecosystem: Services & Support (ACCESS) program which is supported by National Science Foundation grants #2138259, #2138286, #2138307, #2137603, and #2138296 (Allocation PHY230148).

Author contributions

J.M. conceived the research. J.M. performed simulations and data analysis. J.M. and Z.T. interpreted the results. J.M. wrote the paper with contributions from Z.T.

Competing interests

The authors declare no competing interests.

Additional information

Supplementary information The online version contains supplementary material available at <https://doi.org/10.1038/s41524-025-01625-2>.

Correspondence and requests for materials should be addressed to Jaeyun Moon.

Reprints and permissions information is available at <http://www.nature.com/reprints>

Publisher's note Springer Nature remains neutral with regard to jurisdictional claims in published maps and institutional affiliations.

Open Access This article is licensed under a Creative Commons Attribution-NonCommercial-NoDerivatives 4.0 International License, which permits any non-commercial use, sharing, distribution and reproduction in any medium or format, as long as you give appropriate credit to the original author(s) and the source, provide a link to the Creative Commons licence, and indicate if you modified the licensed material. You do not have permission under this licence to share adapted material derived from this article or parts of it. The images or other third party material in this article are included in the article's Creative Commons licence, unless indicated otherwise in a credit line to the material. If material is not included in the article's Creative Commons licence and your intended use is not permitted by statutory regulation or exceeds the permitted use, you will need to obtain permission directly from the copyright holder. To view a copy of this licence, visit <http://creativecommons.org/licenses/by-nc-nd/4.0/>.

© The Author(s) 2025